Colloids and Surfaces A: Physicochemical and Engineering Aspects 676 (2023) 132178

Contents lists available at ScienceDirect

Colloids and Surfaces A: Physicochemical and Engineering Aspects

journal homepage: www.elsevier.com/locate/colsurfa

Ultrafast synthesis of 3D porous flash graphene and its adsorption properties

Yuntian Liao, Rongtao Zhu *, Wenjun Zhang, Pengfei Huang, Yang Sun, Haiyang Zhu

School of Chemical Engineering and Technology, China University of Mining and Technology, Xuzhou 221116, Jiangsu, China

HIGHLIGHTS

- The flash Joule heating can heat the samples in situ.
- It only takes 21 s to synthesize 3D porous flash graphene.
- The removal rate of methylene blue is as high as 99%.

GRAPHICAL ABSTRACT

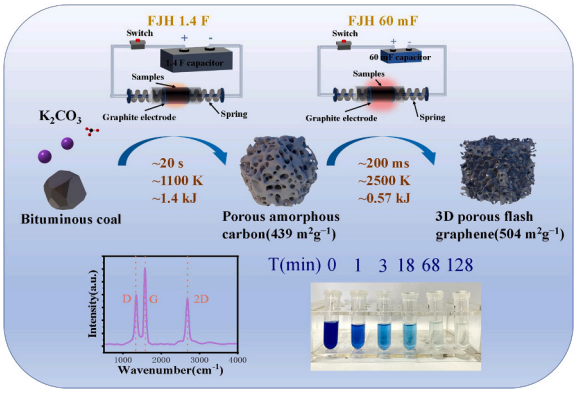

ARTICLE INFO

Keywords:
3D hierarchical porous graphene
Flash Joule heating
Bituminous coal
Adsorption performance
Organic dye

ABSTRACT

3D hierarchical porous graphene (3D HPG) has recently captured significant attention due to its unique porosities, excellent electron transport capability, and multifunctionality. However, given that the traditional preparation method of 3D HPG is time-consuming, energy-consuming and seriously polluting, which seriously block its wide application. This study leveraged the capabilities of flash Joule heating (FJH) to ultrafast synthesize 3D porous flash graphene (3D PFG) with good dispersion and adsorption properties from bituminous coal (BC) within 21 s. The thermal shock generated by carbonate pyrolysis and the thermal expansion generated by Joule heating were used to produce the stable porous structure. Moreover, the specific surface area of 3D PFG was as high as 504 m^2g^{-1}, and displayed the characteristics of hierarchical porous structure of micropores, mesopores and macropores. The porous structure changes of 3D PFG synthesized by FJH under different carbonate ratios and different flash voltages were investigated, and the controllable synthesis conditions of hierarchical pore structures during FJH were obtained accordingly. As the experimental and simulation results show, the 3D PFG displays good dispersibility and good adsorption performance as adsorbent for methylene blue and methyl orange. This environmentally friendly synthetic process of FJH not only simplifies the preparation process of 3D HPG but also provides a valuable way for the high value-added utilization of coal.

* Corresponding author.
E-mail address: rtzhu2010@cumt.edu.cn (R. Zhu).

https://doi.org/10.1016/j.colsurfa.2023.132178
Received 24 April 2023; Received in revised form 31 July 2023; Accepted 1 August 2023
Available online 2 August 2023

1. Introduction

3D hierarchical porous graphene (3D HPG) is widely used in the fields of adsorbents, catalysts and sensors [1–3]. Due to its excellent properties such as stable mechanical properties [4–6], low density [7], excellent electrical conductivity [8,9]and large specific surface area [10,11], it is considered a revolutionary material for the future [12–15]. Compared with other types of graphene, 3D HPG possesses uniformly dispersed active sites due to its high specific surface area, which enhances the ability of interfacial transport and reaction. Its surface and interior can closely interact with organic or inorganic substances [16], endowing it with broad application prospects [17,18]. Especially in water treatment, its unique hierarchical porous structure can shorten the diffusion path and promote the penetration of substances, thus guaranteeing excellent adsorption performance [19,20].

There are various methods for preparing 3D HPG, such as chemical vapor deposition (CVD) [21,22], templated self-assembly [23,24] and chemical redox method [25,26] that have been successfully applied. Zhang et al. prepared graded porous graphene with large specific surface area using polystyrene spheres as a templating agent [27]. Sha et al. prepared sucrose-coated nickel powder to obtain porous graphene oxide after thermal annealing of the particles at 1000 °C [28]. These traditional methods can be broadly divided into two categories according to their synthesis strategies: top-down and bottom-up. Usually, the top-down method is mainly based on the template self-assembly method, using graphene oxide as the raw material, and synthesizing porous graphene under the condition of high temperature, airtight and oxygen deficiency. However, this category requires some special equipment and high temperature confinement conditions, as well as pre-synthesis of nano-etching templates. Accordingly, the synthesis process is long, complex and energy-consuming, and the dispersion and quality of the produced graphene is extremely low [29,30]. As for the bottom-up method (CVD), both the gas source involved in the deposition reaction and the residual gas after the reaction are toxic, and the yield of graphene is as low [31,32]. Therefore, it is crucial to explore the green and efficient synthesis process of 3D HPG.

In order to overcome the disadvantages of the existing 3D HPG preparation methods, such as expensive preparation, tedious synthesis and serious environmental pollution, this study introduced the ultrafast synthesis of 3D porous flash graphene (3D PFG) from bituminous coal (BC) using the flash Joule heating system (FJH). During the FJH synthesis process, due to the internal resistance of the samples itself, the Joule heating can be instantaneously generated by the samples after the two ends of the samples are electrified. Meanwhile, the Joule heating can pyrolyze the activator to activate the samples. In the synthesis process, the discharge time of FJH can be adjusted by changing the capacitance of FJH. First, the sample temperature is gradually increased to 1200 K within 20 s by continuous discharge through FJH (1.4 F). Then through FJH (60 mF) instantaneous discharge, the sample temperature can reach above 2500 K within 200 ms. In this case, the heating and cooling rate of the samples is extremely fast (10^4 Ks^{-1}-10^5 Ks^{-1}). During the FJH process, the thermal expansion and thermal shock effects generated by Joule heating and activator pyrolysis not only increase the degree of graphitization of BC, but also create the hierarchical porous structure in BC. Compared with the original material, the specific surface area of 3D PFG is increased by at least ten times. In addition, the ultra-fast cooling rate avoids the AB stacking of aromatic sheets, resulting in disordered stacking of graphene sheets. The unique turbine layered structure of 3D PFG allows it to maintain the optical and electronic properties of two-dimensional graphene even when hundreds of graphene layers are stacked [33].

Compared with traditional heating devices, FJH is a typical non-radiative heating method. It does not need any carrier such as heating wire or furnace tube to heat the samples, but directly uses the resistance of the samples itself to generate Joule heating in situ. The preparation process is green and convenient, without any strong acid, base or gas. All it needs is to mix the activator and BC and then conduct FJH treatment for 21 s to obtain 3D PFG with good dispersibility. Compared with the traditional synthesis methods, the energy required for the synthesis of 3D PFG is extremely low, only 2 kJ. As the important industrial resource, coal is a natural carbon source with large reserves and high carbon content [34,35]. Compared with biomass carbon sources, coal boasts of the advantages of high synthesis yield and more stable internal structure. Meanwhile, few studies have been conducted on the synthesis of high value-added carbon materials using BC as the carbon source, and even fewer studies on the preparation of 3D HPG using BC. Therefore, the route for the ultrafast synthesis of 3D PFG from BC using FJH has broad application prospects. It not only provides a feasible way for the high value-added utilization of coal, but also has great significance for the reduction of CO_2 greenhouse gas emissions.

2. Experiment

2.1. Chemicals and materials

Deionized water (Sinopharm, AR), Bituminous Coal (Xinjiang, Grain size 75 μm), Carbon black (Cabot, Grain size 150 μm), K_2CO_3 (Sinopharm, AR), Methyl Orange (Sinopharm, AR), Methylene Blue (Sinopharm, AR), Pluronic F-127 (Millipore-Sigma, AR), NaOH (Sinopharm, 0.1 M), HCl (Sinopharm, 0.1 M). All reagents are analytically pure without any treatment.

2.2. The FJH system

The length, outer diameter, and inner diameter of the quartz tube were 50 mm, 8 mm, and 6 mm, respectively. The length and diameter of the graphite electrode were 8 mm and 5.9 mm, respectively. The Quartz tubes and graphite electrodes were purchased from Jiangsu Donghua and Beijing Jinglong, respectively. The FJH system includes a control module, a charging module, a discharging module, a working module, an energy storage module, and a measurement module. In our previous work, the circuit diagram of FJH had been shown [36]. The control module includes a controller PLC and a relay; the charging module includes a charging power supply, a capacitor, a resistor, and a charging switch; The discharging module includes a capacitor, a resistor, and a discharging switch; The energy storage module is mainly composed of a capacitor; the working module includes a sample stage, a reaction box; the measurement module includes a voltage, resistance, and temperature meter. The manufacturer and model for all components were indicated in the Table S1.

2.3. Experimental methods

The 3D PFG synthesis process is as follows: First, BC (75 μm), activator (K_2CO_3), and carbon black (CB) were mixed evenly according to the mass ratio of 1:3:0.04 to obtain the gray powder (KBC). Then 1.5 g of KBC was weighed and put in the quartz tube, with the graphite rod electrodes being put at both ends to block. The compression degree of the samples was controlled by the springs at both ends of the electrode, maintaining the resistance of the sample at about 500 Ω. In the process of FJH treatment, the FJH (1.4 F) was first used to continuously discharge KBC for 20 s (voltage 110 V) to obtain the porous amorphous carbon (PAC). Then the FJH (60 mF) was used for instant discharge (voltage 140 V). In this process, the reaction temperature instantly reached above 2500 K, and the temperature was rapidly lowered to obtain 3D PFG. The samples were washed in deionized water, filtered, and dried at 95 ℃ for 8 h to obtain 3D PFG powder.

2.4. Material characterization

SEM images were taken with a Zeiss Sigma 300 SEM system. A voltage of 10 keV was employed in the process of imaging. TEM and

SAED images were obtained on a JEOL 2100 field emission transmission electron microscope at an acceleration voltage of 200 kV. XPS data were collected using a Thermo Scientific K-Alpha scanning X-ray microprobe with a base pressure of 5×10^{-9} Torr. Survey spectra were recorded using 0.5 eV step sizes with a pass energy of 140 eV. Elemental spectra were recorded using 0.1 eV step sizes with a pass energy of 50 eV. All of the XPS spectra were corrected using the C 1 s peaks (284.8 eV) as reference. Powder XRD spectra were collected with a Bruker D8 advance diffractometer by using zero background sample holders at a scan rate of 2°/min and a 0.1° step size. Raman spectra were collected by a Horiba Raman microscope outfitted with a 532 nm laser. BET surface area analysis was conducted with a Micromeritics APSP2640 BET surface analyzer, with nitrogen as the analysis gas. Samples were degassed for 8 h at 200 °C under a high vacuum prior to analysis.

2.5. Dispersion testing of flash Joule heating porous graphene

F-127 was added to deionized water, and sonicated for 30 min to prepare a 1% F-127 solution. Different quality sample powders (BC, PAC, 3D PFG) and 1% F-127 solution were prepared according to the initial concentration (1 mg/mL∼5 mg/mL) and added to the centrifuge tube. The centrifuge tube was put into the bath sonicator with a power of 480 W (SUNNE, SN-QX-65) and sonicated for 20 min to fully disperse the samples in the solution, and then centrifuged in a centrifuge (ANXIN, ATXG20G) for 5 min at a centrifugal speed of 2000 r/min (447 g relative centrifugal force). Since graphene has strong light absorption, the supernatant was removed by dropper and diluted 100 times. The supernatant was analyzed via ultraviolet–visible spectroscopy (Shimadzu), then the absorbance was recorded at 660 nm, and the concentration of graphene in solution was calculated according to the Lambert-Beer law using the extinction coefficient $\alpha_{660} = 6600\ \mathrm{lg^{-1}m^{-1}}$. The extinction curve was shown in Fig. S1.

2.6. Adsorption properties measurement of flash Joule heating porous graphene

Unless otherwise stated, the experiments in this study were carried out at 298 K, PH= 6 environment (using 0.1 M NaOH and HCl to adjust the pH value). A certain amount of methyl orange and methylene blue dyes was weighed to prepare the dye solution (1000 mg/L), which was then diluted to 200 mg/L. In order to study the adsorption rate of different samples to the dye solution, the samples were added to the 200 mg/L dye solution according to 2 g/L. Then the test tube containing the mixed solution was put into the water bath constant temperature shaking box, and the speed and the temperature of the shaking box was set to 140 r/min and 25 °C, respectively. The solution was removed from the test tube at different time intervals. In order to minimize the loss of dyes, the samples were separated from the solution using the glass fiber needle filter. Then the absorbance of the separated solution was measured at 665 nm and 464 nm by UV-Vis spectrophotometer, respectively. Finally, the removal rate of dyes was calculated (the extinction coefficient of methylene blue is $2.73 \times 10^4\ \mathrm{lmol^{-1}cm^{-1}}$, and the extinction coefficient of methyl orange is $7.72 \times 10^3\ \mathrm{lmol^{-1}cm^{-1}}$).

2.7. Flash Joule heating process simulation

The structure of the flash graphene models was set as follows: The inner diameter and length of the quartz tube of the FJH (1.4 F) models were set to 8 mm and 40 mm, respectively; and the thickness was set to 1 mm. The radius and length of graphite electrodes were set to 8 mm and 10 mm. The radius and length of the intermediate samples were set to 8 mm and 20 mm, respectively. The inner diameter and length of the quartz tube of the FJH (60 mF) models were set to 3 mm and 15 mm respectively, with the thickness set to 1 mm. The radius and length of graphite electrodes were set to 3 mm and 5 mm. The radius and length of the intermediate samples were set to 3 mm and 5 mm, respectively.

Since the current passed through the samples when the FJH was working, Joule heating was generated in situ due to the existing internal resistance, and the samples underwent thermal expansion and deformation. This process involved the multi-physical coupling of electromagnetic heat and thermal expansion. The finite element simulation first used the current physical field, and set the two ends of the material as the discharge voltage plane and the ground plane respectively. The assumption equations (Eqs. (1–3)) used are as follows:

$$\nabla \cdot J = Q_{J\text{-}v} \tag{1}$$

$$J = \sigma E + \frac{\partial D}{\partial t} + J_e \tag{2}$$

$$E = -\nabla V \tag{3}$$

$J$is the current density through the material, $Q_{J\text{-}v}$ is the current source, E is the electric field,σ is the conductivity, D is the electric flux density, t is the FJH synthesis time,J_e is the externally generated current density, V is the electric potential.

Then used the physics of heat transfer in solids, set the external temperature to 293.15 K, and selected the convective heat flux type. The assumption equations (Eqs. (4–5)) used are as follows:

$$\rho C_{\mathrm{p}} \frac{\partial T}{\partial t} + \rho C_{\mathrm{p}} u \cdot \nabla T + \nabla \cdot q = Q + Q_{\mathrm{ted}} \tag{4}$$

$$q = -k \nabla T \tag{5}$$

ρ is the density of the material,C_{p} is the heat capacity of the material at constant pressure,T is the temperature of the material,t is the FJH synthesis time,u is the displacement field vector of the material, q is the heat flux of the material, $Q$is the heat generated under the action of Joule heating,Q_{ted} is the heat generated by the compression or expansion of a material,k is the thermal conductivity,T is the temperature of the material.

Finally, the Young's modulus and Poisson's ratio of each domain were defined by using the physical field of solid mechanics. The assumption equations (Eq. 6) used are as follows:

$$\rho \frac{\partial^2 \mathrm{u}}{\partial^2 t^2} = \nabla \cdot s + F v \tag{6}$$

ρ is the density of the material, u is the displacement field component of the material, t is the FJH synthesis time, s is the stress on the material, F is the deformation gradient, v is the volume of the material. The relevant properties of specific materials were shown in Table S2 below [33].

3. Results and discussion

3.1. Character of flash Joule heating Process

The two-step synthesis of 3D PFG using FJH was demonstrated. The industrial analysis results of BC are shown in Table S3. High fixed carbon content and volatiles endows BC with the potential to transform into 3D PFG. The schematic diagram of FJH device is shown in Fig. 1**(a)**. FJH consists of two capacitor banks of 1.4 F and 60 mF to realize continuous discharge and instantaneous discharge, respectively. The schematic diagram of the FJH process for the synthesis of 3D PFG is shown in Fig. 1 **(b)**. First, the KBC was continuously discharged for 20 s by FJH (1.4 F). Pyrolysis of K_2CO_3 in BC produced a large amount of gas, which mainly caused the thermal shock effect and cracks or even rupture of particles on BC, thus forming the rich hierarchical porous structure including macropores, mesopores and micropores. However, due to the low reaction temperature, the samples could not be graphitized, and PAC ($439\ \mathrm{m^2g^{-1}}$) was obtained. Then FJH (60 mF) was used to discharge PAC instantaneously so that the temperature of the sample could reach up to 2500 K within 200 ms, producing the thermal expansion effect.

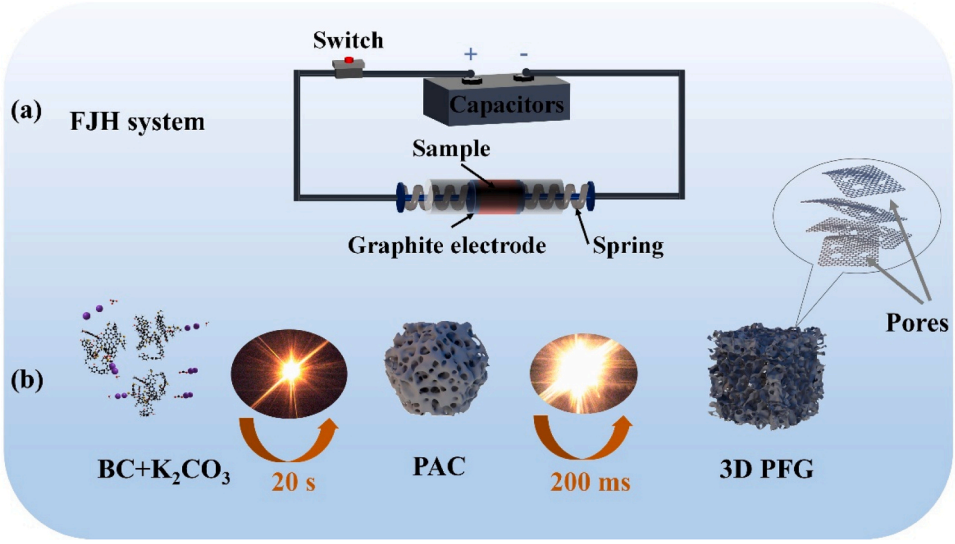

Fig. 1. (a) FJH system (1.4 F and 60mF) schematic; (b) Flow chart of 3D PFG synthesis process.

The remaining activator in the samples were further pyrolyzed, and the porous structure was further increased on the basis of retaining the original hierarchical porous structure. During this ultra-high-speed heating and cooling process (10^4 Ks^{-1}-10^5 Ks^{-1}), the six-membered ring plane composed of carbon atoms underwent continuous decomposition and polymerization, and generated free radicals with high reactivity, which formed graphene-like carbon rings with carbon atoms [33]. Finally, the graphene sheets were stacked disorderly to form 3D PFG (504 m^2g^{-1}).

The electrical signals collected by the FJH process are shown in Fig. 2 (a). The initial voltage of FJH (1.4 F) was 110 V. With the discharge of the capacitor, the current through the samples gradually increased from 0 A to 3 A, and the temperature of the sample gradually increased from room temperature to 1200 K. The energy change of FJH (1.4 F) is shown

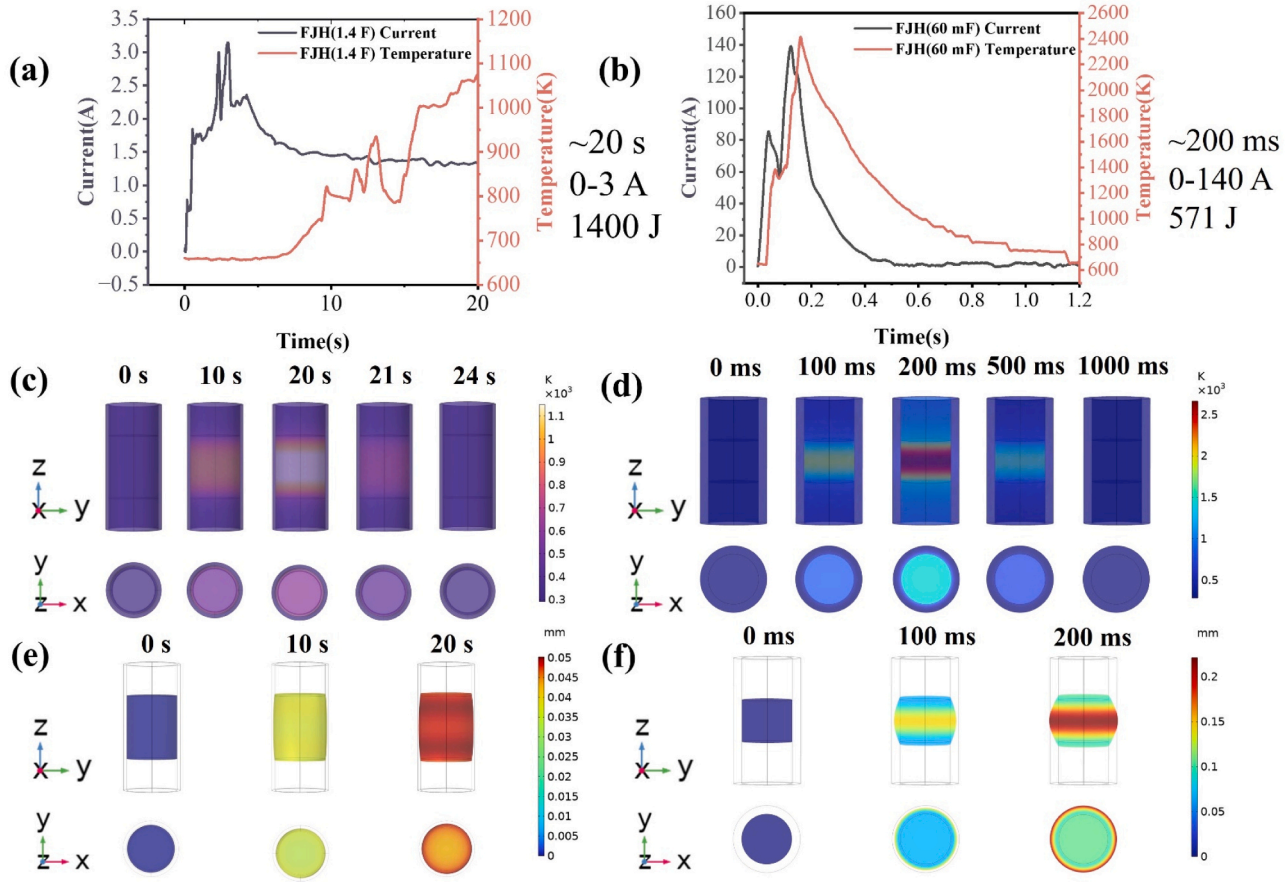

Fig. 2. (a-b) Electrical signal when FJH (1.4 F and 60 mF) work; (c-d) Finite element simulation of temperature variation of synthetic PAC and 3D PFG; (e-f) Finite element simulation of thermal expansion deformation of synthetic PAC and 3D PFG.

in Fig. S2(a). When the discharge lasted for 20 s, about 1400 J of energy was released. The electrical signals collected when the large voltage FJH (60 mF) works are shown in Fig. 2(b), and the initial voltage was 140 V. During the discharge process, a pulse current of about 500 ms could be observed, and the pulse current increased instantaneously from 0 A to 160 A. PAC was also rapidly heated from room temperature to about 2500 K, and cooled to room temperature within one second. The energy change during the reaction is shown in Fig. S2(b). About 571 J of energy was released. These signals indicate that FJH can be rapidly heated in situ under the action of the Joule heating generated by the sample itself, and then rapidly cooled at room temperature; and that the energy consumption during the synthesis process is extremely low. The working process of FJH (60 mF) was recorded by the high-speed camera. As shown in Fig. S3. The Joule heating generated by the samples instantly causes dazzling white light, and the white light intensity reaches the strongest within 200 ms. It can be clearly observed that the electrode is displaced due to the thermal shock and thermal expansion effects produced by the samples, and finally the reaction is finished within one second, and the samples are cooled to room temperature.

In order to investigate the thermal expansion and thermal shock effects during the synthesis process, the finite element analysis of the FJH synthesis process was performed using COMSOL software. The working voltage of synthetic PAC was set to 110 V, and the working voltage of synthetic 3D PFG was set to 140 V. As shown in Fig. 2 (c-d), the temperature when working at low voltage and large capacitance FJH (1.4 F) is much lower than that at high voltage and small capacitance FJH (60 mF). The temperature is the highest at the center of the samples, and gradually declines to the sides. This indicates that the activator pyrolyzes first at the center of the samples and cools down to room temperature in a short time. In order to better display the degree of sample deformation, the sample expansion deformation is shown in the quartz tube, as is illustrated in Fig. 2(e-f). It can be found that when FJH (60 mF) is working, the expansion degree of the samples is significantly greater than that when FJH (1.4 mF) is working. The expansion degree of the samples is proportional to the temperature, and the expansion deformation is most obvious at the center of the highest temperature. However, due to the obstruction of the electrodes at both ends, the deformation of the samples near the electrodes is small. Accordingly, during the FJH reaction process, due to the coupling effect of the electric field and the thermal field, the thermal expansion and thermal shock effect of the sample itself are positively correlated with the expansion and deformation of the samples. The expansion deformation of the actual samples is shown in Fig. S4, which is consistent with the conclusions obtained.

3.2. *Influence of flash Joule heating on microstructure of samples*

Porous structure changes in the samples were observed by SEM. As shown in Fig. 3(a), BC is composed of non-uniform amorphous carbon particles with almost no porous structure. It can be observed in Fig. 3(b) that there are many porous structures of different sizes in PAC, which indicates that the thermal shock effect generated by the pyrolysis of the activator has an active pore-forming effect on the samples. In Fig. 3(c), it can be seen that a large amount of porous structure was preserved in 3D PFG, and there are no amorphous carbon particles, indicating that the porous structure synthesized by FJH is very stable and fully reacted. As shown in Fig. S5, there are only two elements of C and O in 3D PFG. It proves that the temperature of FJH synthesis is higher than the gasification temperature of impurities in BC [36]. Accordingly, the impurities of the samples can be removed so as to ensure the purity of the 3D PFG. In Fig. 3(d-e), the surface of the 3D PFG sheet has a large amount of porous structure. Moreover, the graphene lattice edges can be observed. The lattice spacing of 3D PFG increases to 3.66 Å in Fig. 3(f), which is significantly larger than the 3.34 Å spacing observed in AB graphite [37]. This further proves that the thermal expansion and thermal shock effects generated by FJH can not only increase the porosity of the samples, but also enhance the crystallinity of the samples. In addition, because the disordered stacking between carbon layers expands the interlayer distance, making it easier for the carbon layers to peel off to form the graphene sheet structure. The SAED was used to confirm the

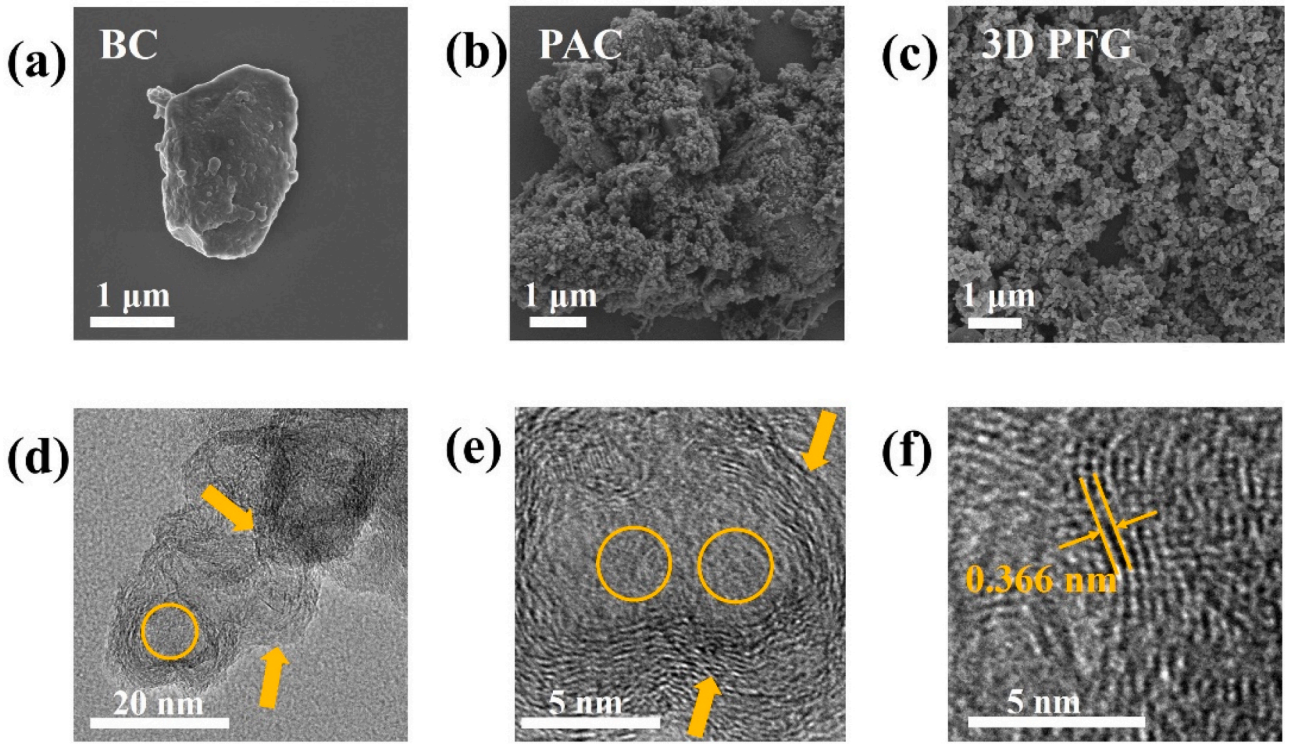

Fig. 3. (a-c) SEM images of the samples before and after the FJH treatment; (d-f) TEM image of 3D PFG, where micropores and mesopores are marked by circles, and graphene sheet structures are marked by arrows.

existence of multiple overlapping crystal lattice in 3D PFG. The (001), (100) and (110) crystal plane structures can be observed in Fig. S6, which proves that the rotation in the carbon layer is disordered.

3.3. Influence of flash Joule heating on chemical composition of samples

The elemental ratio, atomic hybridization mode and surface oxygen-containing functional group type of the samples were analyzed by XPS. As shown in Fig. 4(a-c), with the progress of FJH, the ratio of oxygen to carbon in the samples gradually decreases. This is because BC itself contains some oxygen-containing impurities that are removed after FJH treatment, but due to the pyrolysis of K_2CO_3, the pyrolysis products react with carbon materials to form a small amount of oxygen-containing functional groups [38]. Therefore, while ensuring the high purity of the samples, FJH also leads into a small amount of oxygen-containing functional groups. The presence of oxygen-containing functional groups also provides the basis for good dispersion of 3D PFG. In order to better observe the changes of oxygen-containing functional groups during the flash evaporation process, the XPS fine map of oxygen elements was fitted in Fig. S7. With the progress of FJH, under the action of the high temperature generated by the samples and the pyrolysis of K_2CO_3, the most abundant oxygen-containing functional groups were formed by 3D PFG. It can be observed that the oxygen-containing functional groups correspond to C═O, C-OH and C-O-C, COOH at the binding energies of 531.1 eV, 532.2 eV, and 534.2 eV [39]. To determine the orderliness degree of the samples, the sp^2 hybridization peak and sp^3 hybridization peak can be obtained by fitting the C1s peak [40], as shown in Fig. 4(d-f). The data for the specific fitted peaks are presented in Table (S4–6). During the synthesis process, the peak area ratio of sp^3 to sp^2 and the half peak width of sp^2 gradually decrease. It shows that the hybridization mode of carbon atoms gradually changes from sp^3 to sp^2, and the graphitization degree of the samples after FJH treatment gradually increases.

The graphitization degree of samples during FJH was analyzed by XRD. In Fig. 4(g), the XRD spectrum analysis of BC shows that the diffraction peak of the (002) plane is far away from the typical diffraction peak (26°) of crystalline carbon, while the diffraction peak of the (100) plane hardly exists, and there are messy miscellaneous peaks. This confirms the amorphous carbon structure of BC and the presence of impurities. Compared with BC, the peak intensities of the (002) plane and (100) crystal plane diffraction peaks of PAC increase, and the characteristic peaks of some previous non-carbon impurities disappear, but still remain amorphous carbon structures. In addition, the (002) crystal plane diffraction peak of 3D PFG is the most obvious and the peak line becomes steep. This is because the high temperature generated instantaneously by FJH causes graphitization of PAC. In Fig. S8, the

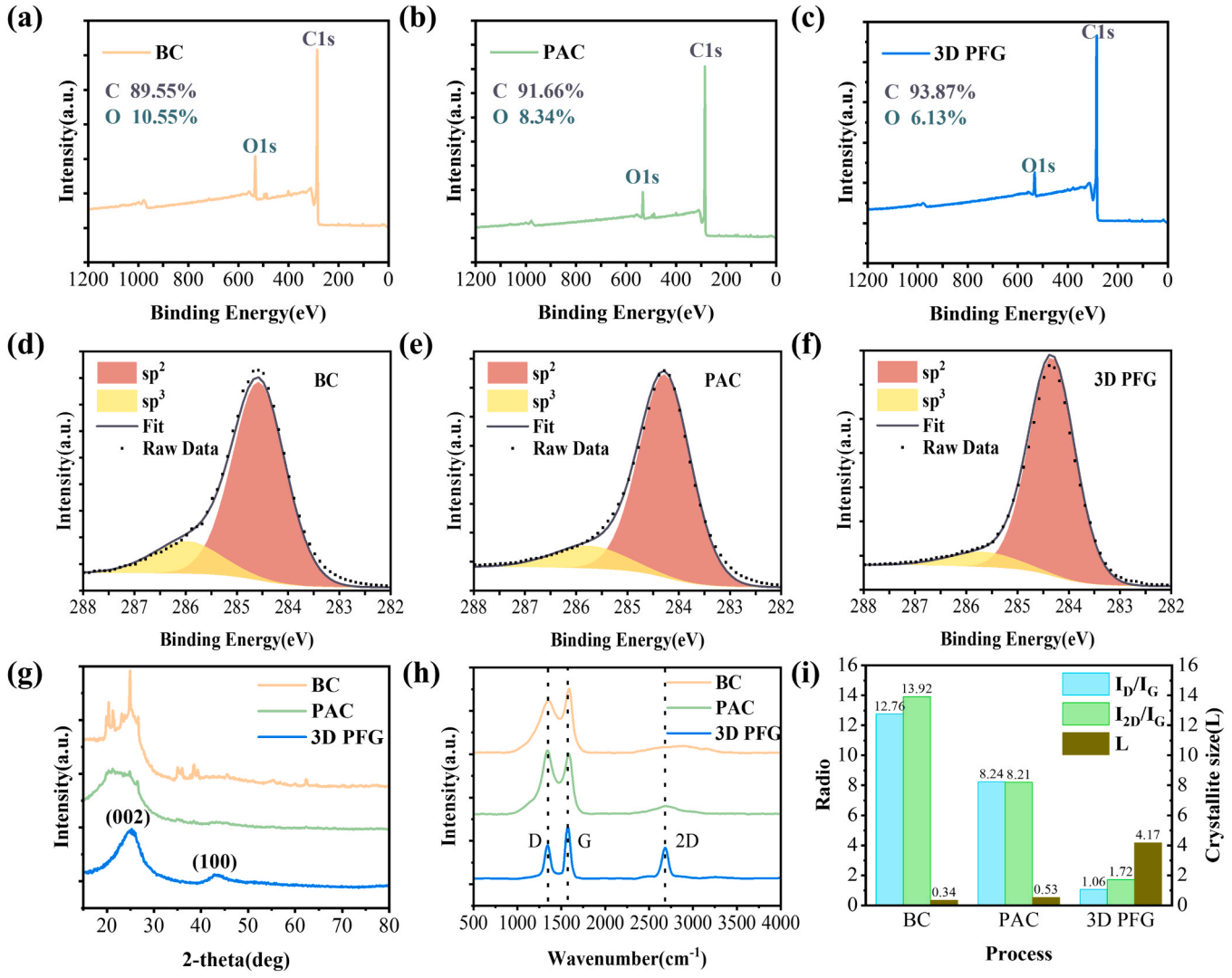

Fig. 4. (a-c) XPS elemental analysis of BC, PAC, 3D PFG; (d-f) Analysis of sp^2 and sp^3 hybridization ratio of BC, PAC, 3D PFG; (g) XRD diffraction patterns of BC, PAC, 3D PFG; (h) Raman spectra of BC, PAC, 3D PFG; (i) I_D/I_G, I_{2D}/I_G and crystallite size L after fitting BC, PAC, 3D PFG Raman spectra.

(002) peak is observed to shift leftward from 26.7° to 25.9° for graphite due to the increase in interlayer spacing. According to the calculation, the interlayer distance of the samples is much larger than 3.34 Å of typical AB stacked graphite. It shows that although the first step of FJH can increase the pores, the synthesis temperature is too low to prevent the samples from graphitization. The instantaneously extremely high synthesis temperature of the second step just compensates this shortcoming and expands the interlayer distance.

Fig. 4(h) reflects the changes of Raman spectra of the samples during FJH. Larger D and G peaks can be seen in the BC [41], and the peak intensity of the 2D peak is very low. This indicates that BC is the amorphous carbon structure. Due to the pores and defects caused by the thermal shock effect in the PAC carbon layer, the peak intensity of the D peak of PAC is increased relative to BC. In contrast, the lower 2D peak is because the synthesis temperature of FJH (1.4 F) is not sufficient to graphitize the samples. As shown in Fig. 4(i), the 3D PFG's I_D/I_G drops to 1.06 and I_{2D}/I_G rises to 1.72. In the synthesis of FJH (1.4 F), the thermal expansion effect produced by the samples makes the activator and impurities to pyrolysis and escape, which further improves the order degree of the samples, and gradually transforms from sp^3 clusters to sp^2 clusters. According to previous studies of graphene, the high I_D/I_G was associated with high sp^3 hybridization and internal defect density, and the high I_{2D}/I_G was associated with high sp^2 hybridization and highly ordered internal structure. But the high I_D/I_G and high I_{2D}/I_G can be observed simultaneously in 3D PFG. However, for the porous graphene in this study, the unusual spectral features observed are due to the presence of abundant porous structures in the highly sp^2 hybridized graphene sheets. The M peak (1750 cm^{-1}) can usually be observed in the Raman spectrum of AB stacked graphite, but this peak type is not found in the spectrum observed, indicating that AB stacking of graphite does not occur.

By analyzing the correlation between the I_D/I_G of Raman spectroscopy and the graphite microcrystal size L (nm) obtained by XRD, the microcrystal base size of the carbon material can be obtained [42].

$$L = 4.4(I_G/I_D) \tag{7}$$

According to the Eq. (7), it can be obtained that the crystallite size of the samples is inversely proportional to I_D/I_G. As the FJH works, the L of the 3D PFG increases to 4.17 nm. It shows that the thermal shock and thermal expansion effect generated by Joule heating cause the amorphous carbon in the samples to interact with each other, so that the crystallite size of the samples gradually increases and transforms into graphene structure.

3.4. Influence of flash Joule heating on the porous structure of samples

When naming the experimental samples, the first two numbers represent the mass ratio of K_2CO_3 to BC, followed by the name of samples, and the last number indicates the flash voltage (3:1–3D PFG_{140}). The porous structure of samples was tested by the Nitrogen Adsorption and Desorption. As is shown in Fig. 5(a), the specific surface area of BC is only 37 m^2g^{-1}, which leads to an unclosed adsorption-desorption curve. The specific surface area of 3:1-PAC_{110} is 439 m^2g^{-1}, and the specific surface area of 3:1–3D PFG_{140} is further increased to 504 m^2g^{-1}. At the same time, a typical type IV nitrogen adsorption-desorption isotherm with an obvious hysteresis loop at relative pressure (P/P_0) from 0.45 to 0.99 is observed in the case of 3D PFG. This indicates that micro- and mesopores exist in 3D PFG [43]. In order to elaborate the change of the pore structure in the samples more clearly, the Density Flood Theory (DFT) model was applied to analyze the pore size distribution of samples. Fig. 5(b) shows that there are almost no micro- and mesopores in BC, and the pore size distribution of PAC is concentrated in micropores (0.8–1.6 nm) and mesopores (2.7–3 nm). However, 3D PFG has the richer hierarchical porous structure. One pore system consists of narrow micropores (0.5–0.8 nm) and the other consists of larger micropores (1–2 nm) and smaller mesopores (2–4 nm). According to the Mean pore-size, 3D PFG also has the macropores. The change in the porous structure of samples during the synthesis of FJH was due to the decomposition of K_2CO_3 into CO and K during the synthesis of FJH (1.4 F). This generated the thermal shock effect and led to the etching of the carbon layer, greatly increasing the porosity of BC, and endowing PAC with the hierarchical porous structure. Then after FJH (60 mF) treatment, the thermal expansion effect caused by the instantaneous ultra-high temperature of PAC further activates PAC, which not only

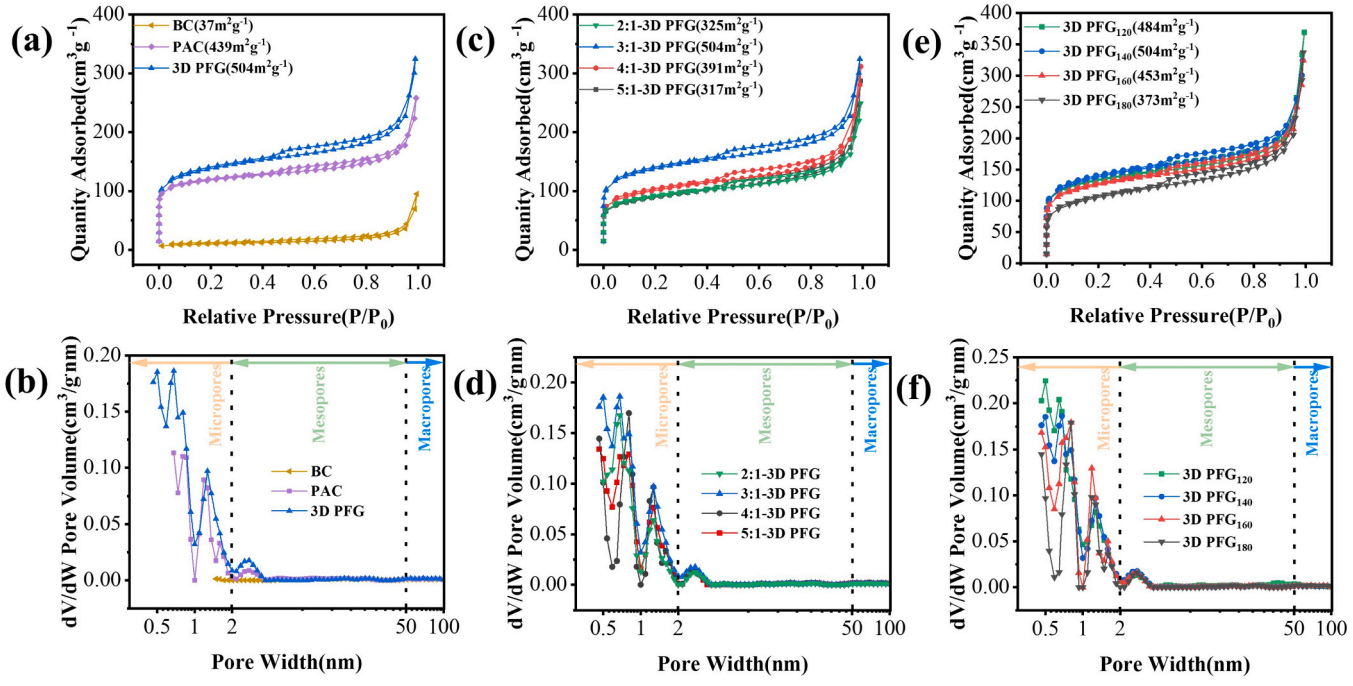

Fig. 5. (a-b) Gas adsorption-desorption curves and pore size distributions of BC, PAC, and 3D PFG; (c-d) Gas adsorption-desorption curves and pore size distributions of 3D PFG_{140} synthesized with different K_2CO_3 ratios; (e-f). Gas adsorption-desorption curves and pore size distributions for 3:1–3D PFG at different voltages.

increases the porosity, but also makes the microporous structure more abundant. The above evidences indicate that FJH can not only increase the porosity of samples, but also generate richer and smaller micropores; and that the synthesized 3D PFG has rich hierarchical porous structure.

It is well known that changes in the hierarchical porous structure of graphene have a non-negligible impact on the adsorption performance of graphene. The micropores ensure the large specific surface area of the samples, which plays a leading role in the adsorption process [44]. Controllable synthesis of FJH porous structure can be achieved by changing the ratio of K_2CO_3 and the size of the flash voltage. In Fig. 5(c), with the increase of K_2CO_3, the porosity of porous graphene shows a trend of increasing first and then decreasing. This is because when the K_2CO_3 content is too low, the pyrolysis products are less and the mixing reaction with the BC is not homogeneous enough to achieve the desired pore-making effect. With the increase of K_2CO_3, the pyrolysis products combined with BC gradually increase, which makes the reaction of the synthesis system more uniform, and the porous structure of the prepared porous graphene more abundant. But when there is too much K_2CO_3, the pores of the samples become larger or even collapse, eventually leading to a decrease in porosity. This result is also confirmed in Fig. 5(d): as the proportion of K_2CO_3 increases, the percentage of micropores gradually decreases. As shown in Figs. S9, 3:1–3D PFG has the highest proportion of micropores, accounting for 54% of the total pore volume.

The effect of synthesis temperature on the porous structure of 3D PFG was explored by changing the flash voltage. In Fig. 5(e), as the flash voltage increases, the specific surface area of 3D PFG first increases and then decreases. When the flash voltage is 140 V, the specific surface area of the samples reaches its maximum. This is due to the fact that the flash voltage affects the synthesis temperature of 3D PFG and ultimately affects the porosity of the samples. When the synthesis temperature at low voltage is too low, it does not allow sufficient pyrolysis of K_2CO_3, resulting in an unsatisfactory activation effect. When the synthesis temperature of high voltage is too high, 3D PFG generates too strong thermal expansion force to collapse the porous structure and reduce the porosity. As Fig. 5(f) shows, with the increase of the flash voltage, the proportion of micropores in 3D PFG tends to decrease gradually. This proves that the temperature also affects the size of micropores during FJH, and the pore size of the micropores gradually becomes larger with the increase of thermal expansion effect caused by Joule heating. Table S7 shows the porous structure properties of 3D PFG for different synthesis parameters. As is shown, the thermal shock and thermal expansion effects generated during the FJH synthesis can be controlled by adjusting the K_2CO_3 content and the flash voltage, thereby achieving control over the porosity and pore size distribution of 3D PFG.

3.5. Dispersibility and adsorption properties of samples at different flash stages

The dispersibility of the samples was determined by measuring the dispersion of the samples in the solution at different times and the concentration of the substance in the solution after centrifugation. As shown in Fig. 6(a), after the samples is dispersed in solution for 5 days, 3D PFG remains well dispersed in solution, while BC and PAC are relatively poorly dispersed. To better judge the dispersibility of the samples, the change of the concentration of the substance after centrifugation was measured and shown in Fig. S10. As can be seen, 3D PFG is still well dispersed in solution after centrifugation. This is due to the spin-disordered graphene structure in 3D PFG. As the pyrolysis of the activator introduces hydrophilic oxygen-containing functional groups, the hydrophilicity of the samples is further improved [45].

To investigate the adsorption properties of the samples, methylene blue was used as the adsorbed dyes. As shown in Fig. 6(b-c), although the adsorption performance of PAC is relatively improved compared with BC, the ideal adsorption effect cannot be achieved due to the existence of amorphous carbon structure and low porosity. Compared with different samples, 3D PFG has the best adsorption effect. In the initial stage of adsorption, the removal rate of 3D PFG to dyes can reach more than 80% in the first few minutes. The adsorption tends to be stable in the later stage, and the dyes can be completely removed in 128 min. This is because 3D PFG not only has the rich porous structure and good dispersion, but also possesses active sites rich in oxygen-containing functional groups. Through surface complexation, hydrogen bonding, and electrostatic attraction, the adsorption of organic pollutants is increased, and the adsorption capacity of organic pollutants is further improved. In order to verify the adsorption performance of 3D PFG on different dyes, methyl orange was used as the dyes. The adsorption effects of samples in different flash stages on methylene orange are shown in Fig. S11. As can be seen, the adsorption rate of 3D PFG to methyl orange can also reach more than 95%, which still shows good adsorption performance. According to the adsorption experiment, it is proved that the adsorption performance of the sample can be greatly improved by FJH.

Fitting analysis of the experimental data for the adsorptions of methyl orange was carried out using the pseudo-first-order model kinetic (Eq. 7), pseudo-second-order kinetic (Eq. 8). The fitting parameters are listed in Table 1 and the fitting results are shown in Fig. 6(d-e).

$$\ln(q_e - q_t) = \ln q_e - K_1 t \tag{7}$$

$$\frac{t}{q_t} = \frac{1}{K_2 q_e^2} + \frac{t}{q_e} \tag{8}$$

q_e (mg/g) is the equilibrium adsorption capacity, q_t (mg/g) is the adsorption capacity, K_1 (min^{-1}) is the quasi-first order dynamic rate constant and K_2 ($g{\cdot}mg^{-1}{\cdot}min^{-1}$) is the quasi-second-order dynamic rate constant were calculated from the slope and intercept of the curves, t is the adsorption time.

It can be seen from Fig. 6(d-e) and Table 1 that the variance of the pseudo-first-order model kinetic model fitting results of the three adsorbents was low and was significantly lower than that of the pseudo-second-order model equation, which cannot describe the characteristics of the adsorption process of the entire adsorbent. Since q_e was calculated by the pseudo-second-order equation, was closer to the experimental value, the pseudo-second-order kinetic model could describe the adsorptions of methylene blue more fully by these three adsorbents. This indicated that the adsorption kinetics of methylene blue by the adsorbents were mainly controlled by chemical adsorption.

The adsorption isotherm is an important criterion to evaluate the adsorption performance of materials. The adsorption isotherms can be described in two general isotherm models including the Langmuir (Eq. 9) and Freundlich (Eq. 10) isotherm models.

$$\frac{C_e}{q_e} = \frac{1}{K_L q_m} + \frac{C_e}{q_m} \tag{9}$$

$$\ln q_e = \ln K_F + \frac{\ln C_e}{n} \tag{10}$$

C_e (mg/L) is the equilibrium concentration of adsorption, q_e (mg/g) is the equilibrium adsorption capacity, q_m (mg/g) is the maximum monolayer capacity of the Langmuir model, K_L is the Langmuir constant, K_F is the Freundlich adsorption equilibrium constant, and n is the adsorption strength.

In Fig. 6(f-k) and Table 2. The Langmuir isotherm equation data revealed that the maximum adsorption capacity (q_m) of 3D PFG was always the highest. According to the fitting results, the R^2 of the correlation coefficients of the Langmuir isotherm equation for the three adsorbents were all higher than that of the Freundlich isotherm equation. This indicated that the adsorption of methylene blue by the adsorbent was more consistent with the Langmuir isotherm model, and the adsorption process belonged to the monolayer adsorption. The adsorption performance of 3D PFG synthesized by FJH was better than the previous research, as shown in the Table 3.

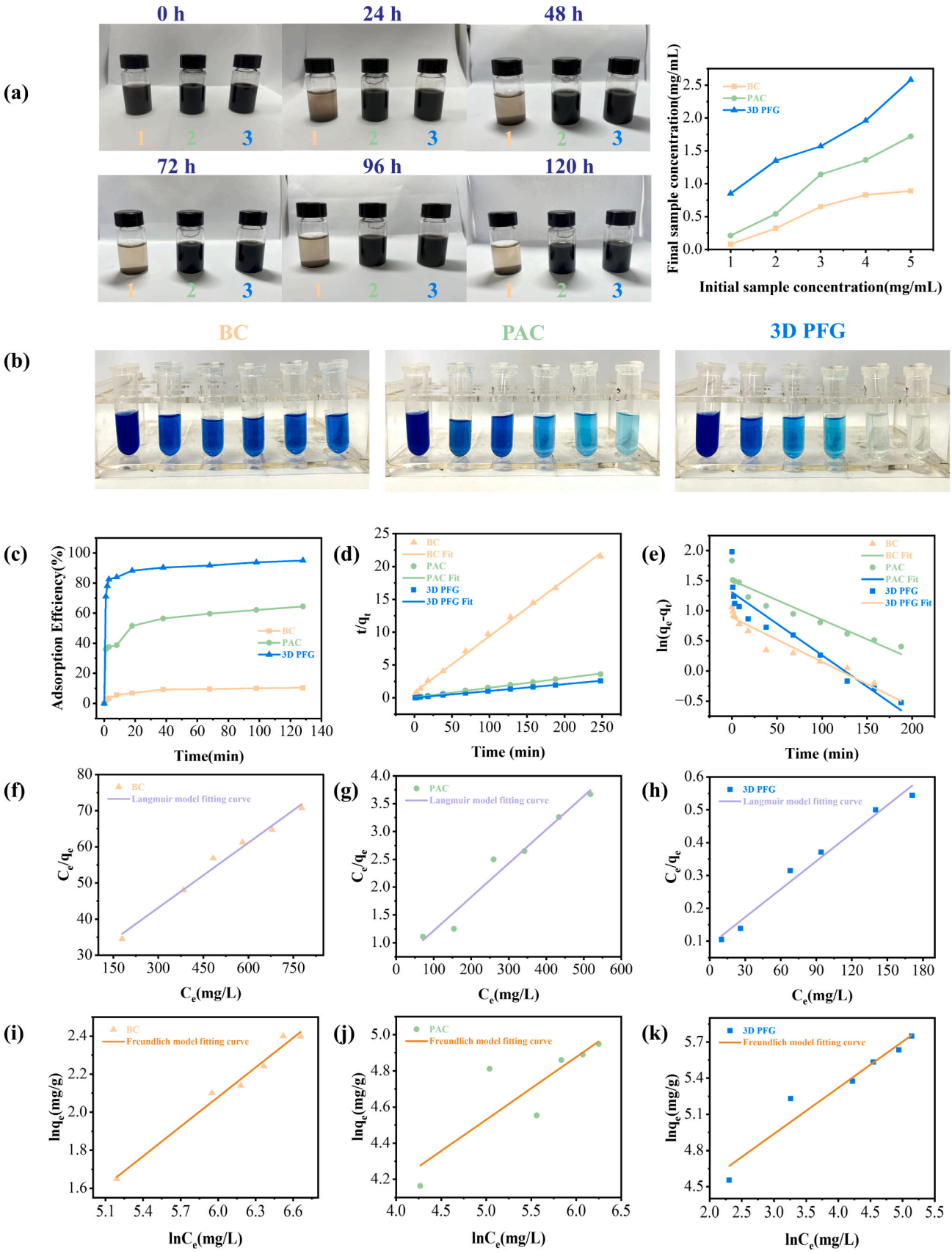

Fig. 6. (a) Comparison of the dispersion of different samples in solution and the change of residual concentration after centrifugation of samples at different initial concentrations (BC, PAC, 3D PFG are numbered 1,2,3 respectively), (b-c) The actual adsorption and adsorption rate of methylene blue by samples at different times, (d-e) Pseudo-first-order and pseudo-second-order adsorption kinetic models for different adsorbents, (f-k) Isotherm models of different adsorbents.

Table 1
Kinetic fitting parameters and experimental adsorption capacities of three adsorbents.

Sample	Pseudo-first-order model			Pseudo-second-order model			
	q_e (mg/g)	K_1 (min^{-1})	R^2	q_e (mg/g)	K_2 (g/mg·min)	R^2	$q_{e.exp}$
BC	2.44	7.41×10^{-3}	0.94	11.71	8.49×10^{-3}	0.99	11.53
PAC	4.50	6.53×10^{-3}	0.91	68.26	2.71×10^{-3}	0.99	68.56
3D PFG	3.70	1.04×10^{-2}	0.88	95.88	7.95×10^{-3}	0.99	95.64

Table 2
Parameters of adsorption isotherm models.

Sample	Langmuir			Freundlich		
	q_m (mg/g)	K_L (L/mg)	R^2	K_F (L/g)	1/n	R^2
BC	15.68	2.53×10^{-3}	0.98	0.36	0.52	0.97
PAC	150.64	1.09×10^{-2}	0.95	16.40	0.35	0.67
3D PFG	368.10	3.09×10^{-2}	0.97	44.26	0.38	0.92

Table 3
Research on the adsorption of methylene blue by coal-based adsorbents in recent years.

Precursor name	Activator	Adsorption capacity (q_m, mg/g)	Reference
Bituminous coal	K_2CO_3	368.10	Current study
Malaysian low rank coal	H_3PO_4	186.4	[46]
Lignite	KOH	151.5	[47]
Anthracite	water steam	61.4	[48]
Kaolinite coal	H_2SO_4	101.5	[49]
Bituminous coal	water steam	340.0	[50]
Bituminous coal	HCL	14.3	[51]
Bituminous coal	water steam	92.6	[52]
Coal-based activated carbon	water steam	375.9	[53]

4. Conclusions

In this study, 3D PFG with good dispersibility and high specific surface area (504 m^2g^{-1}) was successfully synthesized by FJH in a very short time (21 s) using BC as raw material. As was calculated, the energy required for FJH to synthesize 3D PFG was only 2 kJ. The morphology, structure, and chemical composition of samples in different flash stages were characterized and analyzed, and COMSOL was used to perform finite element simulation on the synthesis characteristics of FJH. The results show that 3D PFG has good electronic information of 2D graphene, and the thermal shock and thermal expansion effects during the FJH process are crucial to control the synthesis of hierarchical porous structure. Finally, the adsorption experiments of organic dyes were carried out by using the samples in different flash evaporation stages as adsorbents. It is verified that the 3D PFG prepared by FJH is a green and efficient adsorption material. The convenience of the synthesis and the high quality of the products indicated that the FJH synthesis system is a mass-produced and scalable synthesis method, which significantly simplifies the synthesis process of 3D HPG, not only improves the production efficiency but also ensures the quality, and has important reference significance.

CRediT authorship contribution statement

Yuntian Liao: Conceptualization, Methodology, Validation, Investigation, Writing – original draft, Funding acquisition, Project administration, **Rongtao Zhu:** Investigation, Validation, Writing – review & editing, Funding acquisition, Project administration, **Wenjun Zhang:** Supervision, Writing – review & editing, **Pengfei Huang:** Software, Validation, **Haiyang Zhu:** Software, **Yang Sun:** Investigation.

Declaration of Competing Interest

The authors declare the following financial interests/personal relationships which may be considered as potential competing interests:

Data Availability

Data will be made available on request.

Acknowledgment

This work was supported by National Natural Science Foundation of China (51974307), Key Research and Development Project of Xuzhou City (KC21287).

Appendix A. Supporting information

Supplementary data associated with this article can be found in the online version at doi:10.1016/j.colsurfa.2023.132178.

References

[1] J. Han, I. Johnson, M. Chen, 3D continuously porous graphene for energy applications, Adv. Mater. 34 (2022) 2108750, https://doi.org/10.1002/adma.202108750.
[2] P. Li, W. Wang, F. Su, X. Wang, X. Zhang, X. Zheng, N-doped interconnected porous graphene as advanced electrode material for supercapacitors, J. Alloy. Compd. 893 (2022), 162218, https://doi.org/10.1016/j.jallcom.2021.162218.
[3] X. Zhou, L. Kang, A DFT study of graphene-FeN_x (x=4, 3, 2, 1) catalysts for acetylene hydrochlorination, Colloid Surf. A. 618 (2021), 126495, https://doi.org/10.1016/j.colsurfa.2021.126495.
[4] M. Sivakumar, J. Widakdo, W. Hung, C. Wang, C. Hu, K. Lee, J. Lai, Porous graphene nanoplatelets encompassed with nitrogen and sulfur group for heavy metal ions removal of adsorption and desorption from single or mixed aqueous solution, Sep. Purif. Technol. 288 (2022), 120485, https://doi.org/10.1016/j.seppur.2022.120485.
[5] S. Remanan, N. Padmavathy, S. Ghosh, S. Mondal, S. Bose, N.C. Das, Porous graphene-based membranes: preparation and properties of a unique two-dimensional nanomaterial membrane for water purification, Sep. Purif. Rev. 50 (2021) 262–282, https://doi.org/10.1080/15422119.2020.1725048.
[6] Z. Liang, S. Wang, K. Zhu, Y. Chen, F. Wei, D. Chen, Enhancing the tribological properties and corrosion resistance of graphene-based lubricating grease via ultrasonic-assisted ball milling, Colloid Surf. A. 633 (2022), 127889, https://doi.org/10.1016/j.colsurfa.2021.127889.
[7] T.A. Tabish, F.A. Memon, D.E. Gomez, D.W. Horsell, S. Zhang, A facile synthesis of porous graphene for efficient water and wastewater treatment, Sci. Rep. -Uk. 8 (2018) 1817, https://doi.org/10.1038/s41598-018-19978-8.
[8] M. Sethi, H. Bantawal, U.S. Shenoy, D.K. Bhat, Eco-friendly synthesis of porous graphene and its utilization as high performance supercapacitor electrode material, J. Alloy. Compd. 799 (2019) 256–266, https://doi.org/10.1016/j.jallcom.2019.05.302.
[9] M. Sethi, U.S. Shenoy, D.K. Bhat, Simple solvothermal synthesis of porous graphene-NiO nanocomposites with high cyclic stability for supercapacitor application, J. Alloy. Compd. 854 (2021), 157190, https://doi.org/10.1016/j.jallcom.2020.157190.
[10] Y. Chen, L. Wu, W. Jiang, Y. Liu, P. Li, M. Xiang, J. Chen, Y. Zou, B. Xie, P. Zhang, In-situ synthesis of 3D multifunctional graphene-based layered double oxide composite for the removal of nickel and acid orange, Colloid Surf. A. 657 (2023), 130533, https://doi.org/10.1016/j.colsurfa.2022.130533.
[11] Y. Zhang, H. Zhang, W. Sha, Y. Song, P. Liu, R. Liu, Y. Hou, H. Wei, B. Xu, T. Cao, J. Guo, N-doped graphene nanoribbons intertwined on 3D graphene skeleton as

superior metal-free electrocatalyst for oxygen reduction, Colloid Surf. A. 652 (2022), 129832, https://doi.org/10.1016/j.colsurfa.2022.129832.
[12] M. Sun, S. Huang, L. Chen, Y. Li, X. Yang, Z. Yuan, B. Su, Applications of hierarchically structured porous materials from energy storage and conversion, catalysis, photocatalysis, adsorption, separation, and sensing to biomedicine, Chem. Soc. Rev. 45 (2016) 3479–3563, https://doi.org/10.1039/c6cs00135a.
[13] H. Huang, H. Shi, P. Das, J. Qin, Y. Li, X. Wang, F. Su, P. Wen, S. Li, P. Lu, F. Liu, Y. Li, Y. Zhang, Y. Wang, Z. Wu, H. Cheng, The Chemistry and Promising Applications of Graphene and Porous Graphene Materials, Adv. Funct. Mater. 30 (2020) 1909035, https://doi.org/10.1002/adfm.201909035.
[14] X. Liu, Y. Liu, X. Zhang, X. Miao, 3D graphene/bismuth composite as an efficient catalyst for reduction of 4-nitrophenol, Colloid Surf. A 636 (2022), 128098, https://doi.org/10.1016/j.colsurfa.2021.128098.
[15] H. Huang, F. Fan, Y. Shen, C. Wang, Y. Huang, M. Chern, Y. Wang, L. Wang, 3D poly-ε-caprolactone/graphene porous scaffolds for bone tissue engineering, Colloid Surf. A. 606 (2020), 125393, https://doi.org/10.1016/j.colsurfa.2020.125393.
[16] J.H. Jeong, G. Lee, Y.H. Kim, Y.J. Choi, K.C. Roh, K. Kim, A holey graphene-based hybrid supercapacitor, Chem. Eng. J. 378 (2019), 122126, https://doi.org/10.1016/j.cej.2019.122126.
[17] T. Lekgoba, F. Ntuli, T. Falayi, Application of coal fly ash for treatment of wastewater containing a binary mixture of copper and nickel, J. Water Process. Eng. 40 (2021), 101822, https://doi.org/10.1016/j.jwpe.2020.101822.
[18] N. Yuan, A. Zhao, Z. Hu, K. Tan, J. Zhang, Preparation and application of porous materials from coal gasification slag for wastewater treatment: A review, Chemosphere 287 (2022), 132227, https://doi.org/10.1016/j.chemosphere.2021.132227.
[19] L. Shi, K. Chen, R. Du, A. Bachmatiuk, M.H. Rümmeli, K. Xie, Y. Huang, Y. Zhang, Z. Liu, Scalable seashell-based chemical vapor deposition growth of three-dimensional graphene foams for oil-water separation, J. Am. Chem. Soc. 138 (2016) 6360–6363, https://doi.org/10.1021/jacs.6b02262.
[20] H. Deb, M.Z. Islam, A. Ahmed, M.K. Hasan, M.K. Hossain, H. Hu, C. Chen, S. Yang, Y. Zhang, J. Yao, Kinetics & dynamic studies of dye adsorption by porous graphene nano-adsorbent for facile toxic wastewater remediation, J. Water Process. Eng. 47 (2022), 102818, https://doi.org/10.1016/j.jwpe.2022.102818.
[21] H. Wang, X. Mi, Y. Li, S. Zhan, 3D graphene-based macrostructures for water treatment, Adv. Mater. 32 (2020) 1806843, https://doi.org/10.1002/adma.201806843.
[22] S. Ullah, M. Hasan, H.Q. Ta, L. Zhao, Q. Shi, L. Fu, J. Choi, R. Yang, Z. Liu, M. H. Rümmeli, Synthesis of doped porous 3D graphene structures by chemical vapor deposition and its applications, Adv. Funct. Mater. 29 (2019) 1904457, https://doi.org/10.1002/adfm.201904457.
[23] L. Liu, X. Li, G. Zhang, Z. Zhang, C. Fang, H. Ma, W. Luo, Z. Liu, Enhanced stability lithium-ion battery based on optimized graphene/Si nanocomposites by templated assembly, Acs. Omega 4 (2019) 18195–18202, https://doi.org/10.1021/acsomega.9b02089.
[24] J. Cai, Z. Zhang, S. Yang, Y. Min, G. Yang, K. Zhang, Self-conversion templated fabrication of sulfur encapsulated inside the N-doped hollow carbon sphere and 3D graphene frameworks for high-performance lithium-sulfur batteries, Electrochim. Acta 295 (2019) 900–909, https://doi.org/10.1016/j.electacta.2018.11.013.
[25] R. You, Y.Q. Liu, Y.L. Hao, D.D. Han, Y.L. Zhang, Z. You, Laser fabrication of graphene-based flexible electronics, Adv. Mater. 32 (2020) 1901981, https://doi.org/10.1002/adma.201901981.
[26] F.M. Vivaldi, A. Dallinger, A. Bonini, N. Poma, L. Sembranti, D. Biagini, P. Salvo, F. Greco, F. Di Francesco, Three-dimensional (3D) laser-induced graphene: structure, properties, and application to chemical sensing, Acs. Appl. Mater. Inter. 13 (2021) 30245–30260, https://doi.org/10.1021/acsami.1c05614.
[27] Y. Zhang, Q. Wan, N. Yang, Recent advances of porous graphene: synthesis, functionalization, and electrochemical applications, Small 15 (2019) 1903780, https://doi.org/10.1002/smll.201903780.
[28] J. Sha, C. Gao, S. Lee, Y. Li, N. Zhao, J.M. Tour, Preparation of three-dimensional graphene foams using powder metallurgy templates, Acs. Nano. 10 (2016) 1411–1416, https://doi.org/10.1021/acsnano.5b06857.
[29] Y. Tao, Z. Sui, B. Han, Advanced porous graphene materials: From in-plane pore generation to energy storage applications, J. Mater. Chem. A. 8 (2020) 6125–6143, https://doi.org/10.1039/D0TA00154F.
[30] T. Wang, J. Li, Y. Zhang, F. Liu, B. Zhang, Y. Wang, R. Jiang, G. Zhang, R. Sun, C. P. Wong, Highly ordered 3D porous graphene sponge for wearable piezoresistive pressure sensor applications, Chem. -Eur. J. 25 (2019) 6378–6384, https://doi.org/10.1002/chem.201900014.
[31] X. Wu, F. Mu, H. Zhao, Recent progress in the synthesis of graphene/CNT composites and the energy-related applications, J. Mater. Sci. Technol. 55 (2020) 16–34, https://doi.org/10.1016/j.jmst.2019.05.063.
[32] S. Wang, X. Wang, C. Sun, Z. Wu, Room-temperature fast assembly of 3D macroscopically porous graphene frameworks for binder-free compact supercapacitors with high gravimetric and volumetric capacitances, J. Energy Chem. 61 (2021) 23–28, https://doi.org/10.1016/j.jechem.2021.01.019.
[33] P. Huang, R. Zhu, X. Zhang, W. Zhang, Effect of free radicals and electric field on preparation of coal pitch-derived graphene using flash Joule heating, Chem. Eng. J. 450 (2022), 137999, https://doi.org/10.1016/j.cej.2022.137999.
[34] Z. Jia, B. Lin, How to achieve the first step of the carbon-neutrality 2060 target in China: The coal substitution perspective, Energy 233 (2021), 121179, https://doi.org/10.1016/j.energy.2021.121179.
[35] X. He, H. Zhang, H. Zhang, X. Li, N. Xiao, J. Qiu, Direct synthesis of 3D hollow porous graphene balls from coal tar pitch for high performance supercapacitors, J. Mater. Chem. A. 2 (2014) 19633–19640, https://doi.org/10.1039/C4TA03323J.
[36] P. Huang, R. Zhu, X. Zhang, W. Zhang, A milliseconds flash joule heating method for the regeneration of spent cathode carbon, J. Environ. Sci. Heal. A. 57 (2022) 33–44, https://doi.org/10.1080/10934529.2021.2022422.
[37] M. Zhang, K. Chen, C. Wang, M. Jian, Z. Yin, Z. Liu, G. Hong, Z. Liu, Y. Zhang, Mineral-templated 3D graphene architectures for energy-efficient electrodes, Small 14 (2018) 1801009, https://doi.org/10.1002/smll.201801009.
[38] Z. Xue, J. Wen, C. Yang, L. Yuan, X. Yin, Y. Li, Efficient removal of chloramphenicol by K_2CO_3 activated porous carbon derived from cigarette butts, Biomass-.-. Convers. Bior. (2022) 1–14, https://doi.org/10.1007/s13399-022-02515-z.
[39] S. Chen, T. Luo, K. Chen, Y. Lin, J. Fu, K. Liu, C. Cai, Q. Wang, H. Li, X. Li, Chemical identification of catalytically active sites on oxygen-doped carbon nanosheet to decipher the high activity for electro-synthesis hydrogen peroxide, Angew. Chem. Int. Ed. 133 (2021) 16743–16750, https://doi.org/10.1002/anie.202104480.
[40] B. Lesiak, L. Kövér, J. Tóth, J. Zemek, P. Jiricek, A. Kromka, N. Rangam, C sp^2/sp^3 hybridisations in carbon nanomaterials-XPS and (X)AES study, Appl. Surf. Sci. 452 (2018) 223–231, https://doi.org/10.1016/j.apsusc.2018.04.269.
[41] W. Bao, Z. Wang, B. Hu, D. Tang, Thermal transport across graphene/GaN and MoS_2/GaN interfaces, Int. J. Heat. Mass. Tran. 201 (2023), 123569, https://doi.org/10.1016/j.ijheatmasstransfer.2022.123569.
[42] T. Jawhari, A. Roid, J. Casado, Raman spectroscopic characterization of some commercially available carbon black materials, Carbon 33 (1995) 1561–1565, https://doi.org/10.1016/0008-6223(95)00117-V.
[43] S. Wei, C. Wan, X. Li, J. Su, W. Cheng, H. Chai, Y. Wu, Constructing N-doped and 3D Hierarchical Porous graphene nanofoam by plasma activation for supercapacitor and Zn ion capacitor, Iscience 26 (2023), 105964, https://doi.org/10.1016/j.isci.2023.105964.
[44] H. Cheng, J. Zhang, Y. Chen, W. Zhang, R. Ji, Y. Song, W. Li, Y. Bian, X. Jiang, J. Xue, J. Han, Hierarchical porous biochars with controlled pore structures derived from co-pyrolysis of potassium/calcium carbonate with cotton straw for efficient sorption of diethyl phthalate from aqueous solution, Bioresour. Technol. 346 (2022), 126604, https://doi.org/10.1016/j.biortech.2021.126604.
[45] M. Wang, Q. Li, X. Li, Y. Liu, L. Fan, Effect of oxygen-containing functional groups in epoxy/reduced graphene oxide composite coatings on corrosion protection and antimicrobial properties, Appl. Surf. Sci. 448 (2018) 351–361, https://doi.org/10.1016/j.apsusc.2018.04.141.
[46] A.H. Jawad, S.N. Surip, Upgrading low rank coal into mesoporous activated carbon via microwave process for methylene blue dye adsorption: Box Behnken Design and mechanism study, Diam. Relat. Mater. 127 (2022), 109199, https://doi.org/10.1016/j.diamond.2022.109199.
[47] S.K. Sriramoju, P.S. Dash, S. Majumdar, Meso-porous activated carbon from lignite waste and its application in methylene blue adsorption and coke plant effluent treatment, J. Environ. Chem. Eng. 9 (2021), 104784, https://doi.org/10.1016/j.jece.2020.104784.
[48] B. Purevsuren, Y. Liou, Y. Davaajav, Investigation of adsorption of methylene blue from aqueous phase onto coal-based activated carbons, J. Chin. Inst. Eng. 40 (2017) 355–360, https://doi.org/10.1080/02533839.2017.1308273.
[49] W. Gao, S. Zhao, H. Wu, Direct acid activation of kaolinite and its effects on the adsorption of methylene blue, Appl. Clay Sci. 126 (2016) 98–106, https://doi.org/10.1016/j.clay.2016.03.006.
[50] E.N. El Qada, S.J. Allen, G.M. Walker, Adsorption of methylene blue onto activated carbon produced from steam activated bituminous coal: a study of equilibrium adsorption isotherm, Chem. Eng. J. 124 (2006) 103–110, https://doi.org/10.1016/j.cej.2006.08.015.
[51] S. Banerjee, G.C. Sharma, M.C. Chattopadhyaya, Kinetic and equilibrium modeling for the adsorptive removal of methylene blue from aqueous solutions on of activated fly ash (AFSH), J. Environ. Chem. Eng. 2 (2014) 1870–1880, https://doi.org/10.1016/j.jece.2014.06.020.
[52] M.M.B.Q. Nabi, Adsorption study of methylene blue from aqueous solutions onto bituminous coal based activated carbon, J. Eng. Sci. 13(2) 91–100. https://doi.org/10.3329/jes.v13i2.63729.
[53] D. Xin-hui, C. Srinivasakannan, L. Jin-sheng, Process optimization of thermal regeneration of spent coal based activated carbon using steam and application to methylene blue dye adsorption, J. Taiwan Inst. Chem. E. 45 (2014) 1618–1627, https://doi.org/10.1016/j.jtice.2013.10.019.